Computer Assisted Mechanics and Engineering Sciences, 11: 77–98, 2004.
Copyright © 2004 by Institute of Fundamental Technological Research, Polish Academy of Sciences

Effect of extrusion processing deformation and heat treating on the plastic flow, microstructure, and mechanical behavior of an aluminum alloy

James M. Fragomeni and Sarita Pochampally
The University of Detroit, College of Engineering and Science, Department of Mechanical Engineering, 40001 West McNichols Road, P.O. Box 19900, Detroit, Michigan, USA

(Received July 29, 2002)

The extrusion temperature, extrusion ratio and ram speeds were varied and finite element simulations of the extrusion process were conducted to determine the effect of these extrusion parameters on temperature transients, strain rate, and metal flow uniformity for the high temperature plastic deformation of an aluminum-lithium alloy billet. The finite element simulations were important in determining temperature transients, metal flow patterns, and the distributions of strain and strain rate during the extrusion process. The contours showed that the strain, strain rate and metal flow were not uniform but varied as the billet was extruded; this might be due to the non-uniform distribution of temperature during the extrusion of the billet. The microstructure of the aluminum-lithium alloy was computer simulated and correlated to the processing parameters and flow stress based on the heat treating times and temperatures. The extrusion processing variables were correlated to the Zener–Hollomon parameter temperature compensated strain rates. Extrusion temperature and extrusion ratio were found to have very little effect on the strength or ductility. The as-extruded section geometry was found to have the largest effect on the strength and ductility.

1. Introduction

The extrusion of a material is a very complex process since it involves the interaction between the material properties and the processing variables. The extrusion process is often used to produce a section geometry that must satisfy strict geometric, microstructural, and property specifications. There are several processing variables which can be controlled during an extrusion process. These variables include the extrusion ratio, the extrusion temperature, the strain rate, and the ram speed. However, the extrusion ratio is often pre-determined by the product specifications so that only extrusion temperature and ram speed are controllable. A material is extruded when it is reduced in cross section by forcing it through a die under high pressure. Most metals are extruded at elevated temperatures since the deformation resistance is low and therefore less force and energy are required to force the extruded billet through the die orifice. The extruded billet is forced through the die orifice by a ram with a dummy block or pressure plate at the end of the ram in direct contact with the billet. On addition to changing the shape of the material, the extrusion process also has a substantial influence on the microstructure and properties. The plastic deformation of the metal i.e., the metal flow that occurs during the extrusion process alters the grain size, texture, subgrain size, dislocation density and various other microstructural features. Often the material being extruded is not homogeneous in structure and properties, therefore variations in the microstructure and properties occur across the cross-section of the final extruded product. The mechanical properties and microstructure can also vary with length since the temperature is hard to maintain constant throughout the extrusion process. The extrusion temperature often varies from the heat generated during the extrusion process. Heat is conducted from the billet to the extrusion container, tools, and ram.

The alloy that was extruded for this study was an aluminum alloy containing 2.6wt. % lithium and 0.09wt. % zirconium. This alloy was strengthened by heat treatment causing nucleation, growth, and coarsening of coherent metastable δ' (Al_3Li) precipitates in the microstructure. The δ' precipitates which are a consequence of artificial aging the Al-Li alloy, are spherical, ordered, and coherent with the aluminum matrix and impede the dislocation glide motion during plastic deformation. The δ' particles grow homogeneously in the matrix, and have the Cu_3Au ($L1_2$) superlattice crystal structure. In general, aluminum-lithium alloys are used primarily for aerospace structural applications since they have attractive properties such as a lower density and higher elastic modulus than conventional non lithium containing alloys.

2. Material processing

An aluminum-lithium alloy having a composition of 2.6wt. % lithium and 0.09wt. % zirconium (see Table 1) was cast by the Aluminum Company of America, ALCOA laboratories, in the form of a rolling ingot slab. One large ingot was cast having the dimensions of 30.5 cm (12 in.) X 96 cm. (38 in.) X 30.5 cm. (12 in.). The ingot was later preheated in a gas fired furnace at the ALCOA Extrusion Works, Lafayette, Indiana, for eight hours in the temperature range of 482–500° C (900–925° C) followed by 12 hours in the temperature range of 527–538° C (980–1000°F). Several smaller billets were then machined from the one preheated larger ingot to be used for the extrusion processing.

Table 1. Composition analysis determined by optical emission spectrometric analysis for the Al-Li-Zr research alloy

Al	Li	Zr	Cu	Mg	Si
bal	2.59	.09	.11	.07	.04

Fe	Ti	B	Na	Ca
.03	.01	<.001	<.001	<.001

2.1. Extrusion parameters

From the preheated ingot, billets 15.25 cm (6 in.) diameter and lengths of either 25.4 cm. (10 in.) or 50.8 cm (20 in.) were machined. The aluminum-lithium billets were direct extruded by the ALCOA Lafayette Extrusion and Tube Division, Lafayette Indiana, after being reheated to temperatures of either 466° C (870°F) or 290° C (555°F). Six product geometries, three round rods and three rectangular sections, were extruded from the billets using an instrumented 2500 ton press in the direct mode.

2.2. Extrusion post-processing/heat treating

The Al-Li alloy was machined into standard ASTM tensile samples from the extruded product. All of the tensile samples were oriented in the longitudinal grain direction. The tensile specimens were solution heat treated for one hour at 550° C (1022°F) in a molten sodium nitrate salt solution followed by a cold water quench to room temperature. Following the solution heat treatment, the tensile samples were artificially aged for various lengths of time in a molten sodium nitrate ($NaNO_3$) salt bath, followed again by a cold water quench. Different artificial aging treatments were utilized by varying both aging time and the aging temperature. Most of the tensile samples were aged at temperatures of 185° C (365°F) and 193° C (379°F). The molten salt solution was continuously stirred throughout the solution heat treatment and aging process to insure a uniform temperature distribution throughout the salt bath.

3. Metallography and microstructure

In order to study the grain structure of the alloy, light optical microscopy (LOM) was performed on samples that were fine ground and mechanically polished to 0.05 μm. The sequence of the mechanical polishing was as follows; (1) 240, 320, 400 and 600 grit SiC paper; (2) 600 grit alundum; (3) 0.5 μm alumina and (4) 0.05 μm MgO slurry. The specimens were anodized and then observed under polarized light to reveal the grain structure. Anodization was performed in a solution containing 948 ml deionized H_2O, 55 ml HBF_4, and 7 grams H_3BO_3 (Boric Acid) for one minute at 18 volts and −32° C. Representative polarized light micrographs were then taken of the partially recrystallized grain structure in the peak-aged condition of 48 hours aging time at 185° C aging temperature in the longitudinal and transverse directions as seen by Figs. 1a and 1b, respectively.

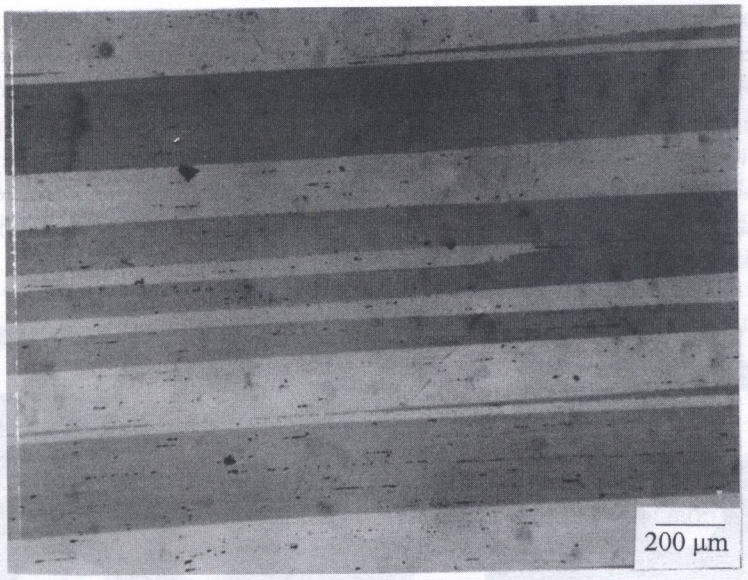

Fig. 1a. Light optical micrograph showing the grain structure for the solution heat treated condition of the Al-2.6wt. % Li-0.09wt. % Zr alloy showing the longitudinal direction

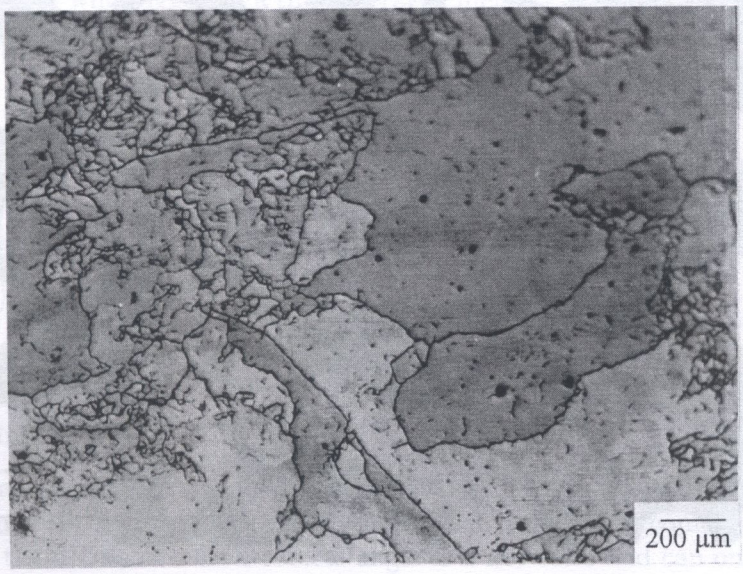

Fig. 1b. Light optical micrograph showing the grain structure for the solution heat treated condition of the Al-2.6wt. % Li-0.09wt. % Zr alloy showing the transverse direction

The particle size distribution and particle morphology were examined and photographed using transmission electron microscopy (TEM) from thin foil specimens obtained from samples aged at 185° C for various aging times ranging from 24 to 225 hours. The thin foil specimens were sliced with a diamond saw cutter and then polished to foils approximately 0.05 mm thick. Disks approximately 3 mm in diameter were then punched from the foils. The thin foil disks were then electropolished using a twin jet polisher, with the disks submerged in a 3:1 methonol-nitric acid solution (the electrolyte) and cooled by liquid nitrogen to around −20 to −35° C. The thin foil disks were observed and photographed using a JEOL-200 CX microscope operating at 200 KV for various specimen inclinations. Centered dark field images were used since they gave good contrast between images of the δ' particles and the matrix phase (see Fig. 2). Particle size measurements of both the Al_3Li precipitates and composite Al_3Li-Al_3Zr precipitates were performed directly from TEM negatives. A semiautomatic eyecom II image analyzing system was used to measure the particle sizes. The average particle size was measured for each aging time. Particle size distributions of over 500 particles were constructed for each aging time. Two particle diameters were measured for each particle in order to determine the aspect ratio of each particle, and thus quantitatively describe the spherical morphology of the particle size distributions. The δ' particle precipitation response in the microstructure was a direct result and consequence of the heat treating artificial aging practice that was done on samples of the extruded alloy after the extrusion was completed. In addition at lower magnifications, the subgrain sizes were also studied directly for various aging conditions using transmission electron microscopy.

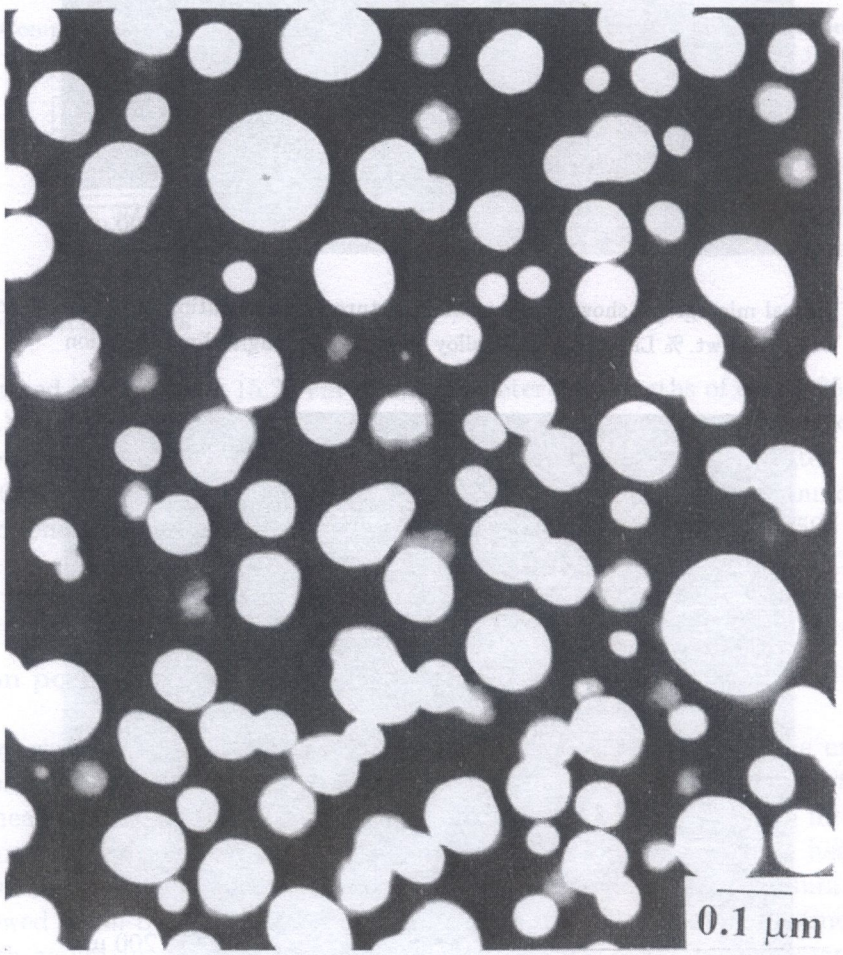

Fig. 2. Transmission electron micrograph dark field image showing the microstructure of the Al-2.6wt. % Li-0.09wt. % Zr demonstration alloy in the overaged condition, aged at 185° C for 96 hours, (200,000X), from thin foil specimens

4. Background on extrusion processing

4.1. Estimating the average equivalent extrusion temperature

The relative motion between the billet and the container wall which cause heat to be generated during direct extrusion, also causes some plastic deformation. Thus the exit temperature of the extruded product will often be greater than the initial temperature of billet prior to extrusion. The rise in temperature causes the variations in the temperature of material perpendicular to and transverse to the ram travel. Transverse variations in temperature produce variations in structure, and hence in properties, across to extruded geometry. Therefore, in order to accurately represent the extrusion temperature for the given extrusion process, an average equivalent extrusion temperature, developed by Farag and Sellers [1], is often used to show this relationship and is expressed as

$$T_{\text{eq}} = (2T_oT_f)/(T_o + T_f) \tag{1}$$

where T_o is the initial billet temperature, T_f is the exit extrusion temperature or the final billet temperature, and T_{eq} is the average equivalent extrusion temperature. Thus the general rise in temperature during extrusion can cause variations in the internal structure and properties of the extruded product. Thus, based on the exit extrusion temperatures and the initial billet temperatures, the equivalent extrusion temperatures were calculated and used for the analysis. Based on the equivalent extrusion temperatures, the Zener–Hollomon parameters were determined and used to establish the relations between extrusion processing and microstructure and mechanical properties. The extrusion temperature was found to have little effect on the strength or ductility.

4.2. The approximate average strain rate

There are several factors that can influence the strain rate of a material during extrusion such as lubrication and temperature. Both the strain and strain rate during extrusion are not constant nor independent of position [2, 3]. Investigators making use of partially extruded billets clearly show that the microstructure is inhomogeneous with a heterogeneous strain distribution across the cross section. Due to the heterogeneous strain distribution it is necessary to calculate a mean or average equivalent strain rate in order to relate the processing variables to the microstructure and bulk properties of the extruded product. The most common approach used to calculate this value was developed by Feltham [4], who suggested a time-averaged method based on the relationship given by

$$\varepsilon' = \text{total strain/time to produce the strain} = \varepsilon/t \tag{2}$$

with the total strain ε given by

$$\varepsilon = \ln(\chi R_e), \tag{3}$$

where R_e is the extrusion ratio, and χ is the shape factor for noncircular extruded product. The time required to yield the total strain is expressed as

$$t = D/\{6V \tan\alpha\}, \tag{4}$$

where V is the ram speed, α is the semiconical die angle, and D is the billet diameter. Combining Eqs. (2) through (4) gives the approximate expression for the mean equivalent strain [5]

$$\varepsilon' = \{6V \tan\alpha\}\{\ln(\chi R_e)\}/D, \tag{5}$$

where ε' is the average equivalent strain rate. A semi-conical die angle α based on the extrusion geometry of the round rods was chosen for this study. Since not all the geometries produced in this study were circular, the notion of a semi-conical angle α is not valid and can only be considered as an approximation for the non-axisymmetric extrusions. Table 8 summarizes the calculated values for the average equivalent extrusion rate for the values of the extrusion parameters corresponding to the Al-2.6wt. % Li-0.09wt. % Zr alloy.

4.3. Estimating the Zener–Holloman parameter

The flow stress during plastic deformation depends on the applied processing variables. These variables include the strain rate or rate of deformation and the temperature of plastic deformation, and can be related to material constants by the Zener–Hollomon parameter (Z). Mathematically the Zener–Hollomon parameter or temperature compensated strain rate can be expressed by the expression given by [1, 6]

$$Z = \varepsilon' \exp\{Q_{\text{flow}}/RT\} = A[\sin h(\beta\sigma)]^n \tag{6}$$

where ε' is the mean equivalent strain rate, Q_{flow} is the activation energy for deformation or plastic flow, R is the universal gas constant, T is the extrusion temperature, σ is the flow stress, and A, β, and n are empirical constants. The calculated Zener–Hollomon parameters are summarized in Table 3 for the extrusion processing of the Al-2.6wt. % Li-0.09wt. % Zr alloy based on the appropriate values for ε, Q_{flow}, R, and T.

4.4. The activation energy for plastic flow

The activation energy for plastic flow, Q_{flow}, is the activation energy necessary for plastic deformation and is dependent on the particular metal or alloy. The activation energy for plastic flow or deformation is approximately equal to the activation energy for self diffusion in high stacking fault alloys [7]. The activation energy is to a small extent a function of the alloy composition. However, Castle and Sheppard [2] determined that Q_{flow} ranged from 156 to 164 KJ/mole for a large range of compositions of aluminum alloys, and concluded that it does not appear necessary to obtain a highly accurate value of the activation energy for the study of high temperature deformation. For commercially pure aluminum, Farag and Sellars [1] derived an activation energy value of 150 KJ/mole. Other investigators [6,8] determined a value for the activation energy to be approximately equal to 155 KJ/mole. For the Al-2.6wt. % Li-0.09wt. % Zr alloy used in this investigation, an average value of the activation energy of 160 KJ/mole [2] was used as the approximate value for Q for the binary Al-Li alloy throughout this study for the calculations of the temperature compensated strain rate.

4.5. Correlation of Z with measured microstructure grain size

The Zener–Hollomon parameter, Z, can be related to the subgrain size of the high temperature deformed aluminum alloy. By relating the Zener–Hollomon parameter to the development of the subgrain structure correlations can be made to the processing parameters such as the billet temperature, strain rate, and exit extrusion temperature. The subgrain size of hot worked aluminum is found to be uniquely related to Z by equations of the form [9, 10, 11]

$$d_{\text{sg}}^{-1} = a_{\text{sg}} + b_{\text{sg}} \ln(Z) \tag{7}$$

where d_{sg} is the average subgrain size, Z is the Zener–Hollomon parameter, and a_{sg} and b_{sg} are empirical constants. Using linear regression techniques and the examination of subgrain sizes along with the calculated values of Z, the constants a_{sg} and b_{sg} can be determined. Thus, using Eq. (7) for the Al-2.6wt. % Li-0.09wt. % alloy in the as-extruded condition the values for the constants a_{sg} and b_s were determined as $a_{\text{sg}} = -1.2$, and $b_{\text{sg}} = 0.06$. For the Al-2.6wt. % Li-0.09wt. % alloy in the solution heat treated condition $a_{\text{sg}} = -0.5$, and $b_{\text{sg}} = 0.03$. Thus, increases in the subgrain size with solution heat treating as compared with the as-extruded resulted in higher Z values and less stable substructure.

Figure 3 shows the dislocation subgrain structure for the Al-Li alloy in the peak-aged condition. The dislocation subgrain sizes were obtained directly from TEM micrographs. In the peak-aged condition, the average dislocation substructure grain size diameter was measured to be approximately

4.58 μm for the peak aged heat treatment (48 hours at 185° C), based on several diameters measured for each subgrain. However, even though subgrain size could be correlated to processing parameters, the subgrain size had a negligible effect on the tensile properties. In Al-Li alloys the strengthening is primarily a consequence of plastic deformation from dislocation δ' particle interactions and thus any strengthening effect from the dislocation subgrain structure is very small in comparison.

Fig. 3. Dark field TEM micrograph showing the dislocation subgrain structure of the Al-2.6wt. % Li 0.09wt. % Zr Alloy in the peak-aged condition, artificially aged at 185° C for 48 hours, (12000X), from TEM thin foil specimens

5. Precipitation results

5.1. The particle size, growth rate, and size distribution

To develop a model for predicting the precipitation hardening response, the particle size distribution, and the average particle size, for each given aging time along the age hardening curve must be determined. For aluminum-lithium alloys, the precipitates coarsen according to the Lifshitz–Slyozov–Wagner (LSW) coarsening theory even at very small sizes [12, 13]. The following Eqs. (8) through (24) were used to predict and simulate the microstructure of the Al-Li alloy as illustrated by Figs. 4 and 5. The average particle size can therefore be determined from the Lifshitz–Slyozov–Wagner [14, 15] cubic coarsening theory which can be expressed by the relation

$$\bar{r}^3 - r_o^3 = K_c t \tag{8}$$

where r_o is the initial particle size (at $t = 0$) and can be taken as approximately equal to zero for the Al-Li demonstration alloy. The growth rate constant K_c at small volume fractions K_{co}, is given by the expression [14, 15].

$$K_{co} = \frac{8\gamma V_m^2 C_{eq} D}{9RT} \tag{9}$$

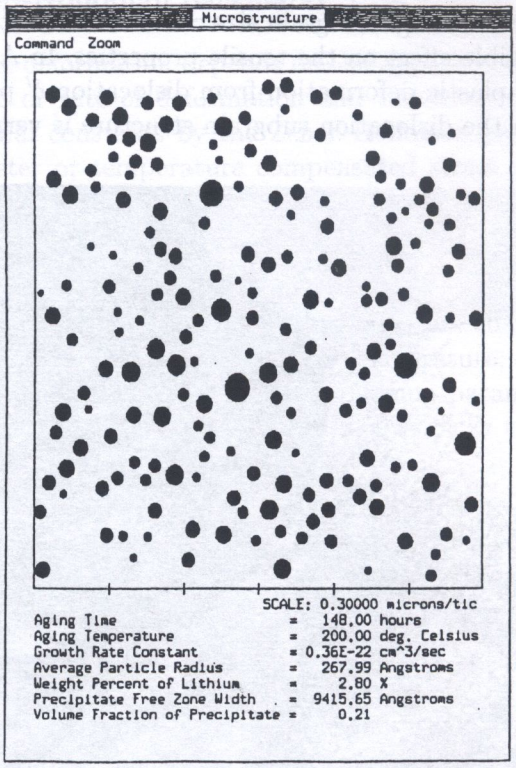

Fig. 4. Computer simulated TEM microstructure for a binary aluminum-lithium, Al-2.8wt. % Li, alloy precipitation age hardened for 148 hours at 200° C, showing the distribution of Al_3Li (δ') precipitates in the matrix phase of the overall microstructure

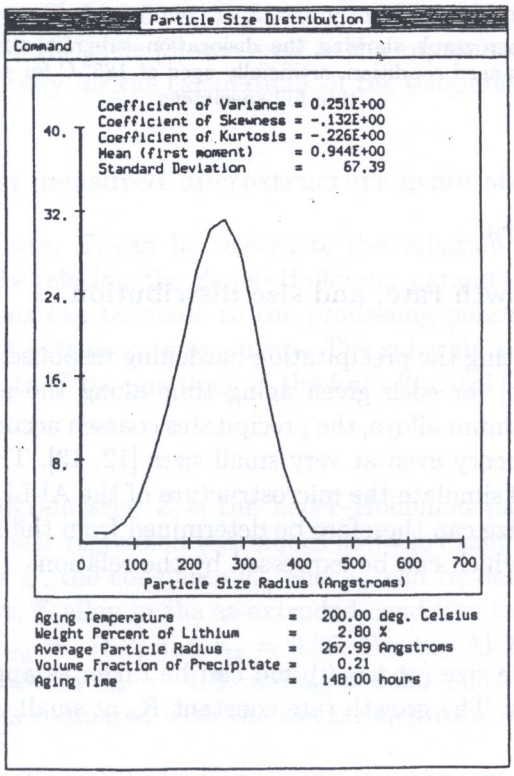

Fig. 5. Computer simulated particle size distribution showing the size distribution of δ' (Al_3Li) precipitates for an Al-2.8wt. % Li alloy artificially aged at 200° C for 148 hours

where T is the aging temperature, R is the universal gas constant, K_{co} is the rate constant, D is the diffusion coefficient, γ is the interfacial energy, C_{eq} is the equilibrium concentration of the solute in the matrix, and V_m is the molar volume of the precipitate. It is known that this expression for K_{co} is valid for very small volume fractions while supposedly more realistic rate constants are dependent on $f_{\delta'}$ [16, 17]. There have been modifications [17, 18, 19] to the LSW model given in Eq. (8) to take into account the volume fraction dependence of the coarsening rate. For example, Ardell [17] modified the LSW theory to account for the high volume fraction effect on K_{co} in some alloys. The modified version of the LSW theory is referred to as the modified LSW (MLSW) theory and can be expressed in terms of the rate constant as [17]

$$K_{fv} = \frac{6\gamma V_m^2 C_{\text{eq}} D}{RT} \frac{\overline{\rho}_{fv}^3}{v_{fv}} \tag{10}$$

and

$$\frac{\overline{\rho}_{fv}^3}{v_{fv}} = \frac{4K_{fv}}{27K_{\text{co}}} \tag{11}$$

where K_{fv} is the growth rate constant at a given volume fraction of f_v, f_v is the total volume fraction of the precipitates in the microstructure, K_{co} is the growth rate at very small volume fractions, $\overline{\rho} = \overline{r}/r_c$ is the relative radius, ρ_{fv} is a function related to volume fraction and a constant times $\mathrm{d}t/\mathrm{d}r_c^3$ and r_c is the critical particle radius of the polydisperse system [17]. When $f_v = 0$, then $\rho_{fv} = 27/4$, and Eq. (10) reduces to the LSW theory, Eq. (9) [17, 20]. The growth rate can also be expressed in terms of the activation energy for diffusion given by the relation [21]

$$K_c = \frac{C_k}{T} \exp\left[\frac{-Q_A}{RT}\right] \tag{12}$$

where Q_A is the activation energy, T is the aging temperature, C_k is the kinetic constant, and R is the universal gas constant. The cubic coarsening expression can therefore be expressed by the relation [14, 15, 21]

$$\overline{r}^3 - \overline{r}_o^3 = \frac{C_k t}{T} \exp\left[\frac{-Q_A}{RT}\right]. \tag{13}$$

Alternatively, the growth rate can be written in terms of the composition and aging practice for the Al-Li demonstration alloy. Based on the microstructural model [20, 22–29] along with some data generated by some other investigators [30, 31] a simple empirical expression relating lithium content, aging temperature, and aging time may be determined as [32]

$$\ln\{K_c T\} = \frac{b}{T} + c \tag{14}$$

where b and c can be expressed as functions of lithium content given by [32]

$$b = -2545.73(\text{wt.}\,\%\,\text{Li}) - 4749.06, \tag{15}$$

$$c = 5.88(\text{wt.}\,\%\,\text{Li}) - 36.87. \tag{16}$$

These simple expressions permit the calculation of the particle size for the demonstration alloy based on the aging practice and composition parameters [32].

For Al-Li alloys, the particle size distribution can be modelled with the Weibull distribution [20, 22–29, 32, 33] which has the form given by

$$P(x) = ghX^{h-1} \exp\left(-gX^h\right) \tag{17}$$

for $X > 0$, $g > 0$, and $h > 0$

$$P(x) = 0 \text{ elsewhere} \tag{18}$$

and

$$\int_0^\infty P(X)\mathrm{d}X = 1 \tag{19}$$

where $P(X)$ is the Weibull probability density function, g and h are the Weibull parameters, and X, which is the normalized particle size diameter, is the ratio of the ith particle diameter d_i to the average particle size diameter $\overline{d}$ for each determined particle size distribution along the precipitation hardening curve. X is also equivalent to the ratio of the ith particle radius r_i to the average particle size radius $\overline{r}$ of each particle size distribution along the precipitation hardening curve. For the Al-Li demonstration research alloy, the values for the Weibull parameters can be determined from the empirical relations given by [20, 22–29, 32, 33,]

$$g = 0.94 - 0.03(\text{wt.\% Li}), \tag{20a}$$

$$h = 5.80 - 0.52(\text{wt.\% Li}) \tag{20b}$$

where g and h are the Weibull distribution parameters given in terms of the weight percent lithium. The equations can also be expressed in terms of the volume fraction of precipitates given by [2, 3, 26, 30–37]

$$g = 0.88 - 0.12 f_v, \tag{21}$$

$$h = 4.69 - 2.17 f_v \tag{22}$$

where g and h are expressed in terms of the volume fraction of the δ' precipitate phase in the matrix. These Weibull parameters, g and h, are most applicable for the heat treating of binary Al-Li alloys such as the demonstration alloy described in this research. Figure 4 shows an example of a computer simulated microstructure using Eqs. (17) through (22) based on a Weibull particle size distribution of approximately 200 different particle sizes. Figure 5 shows the corresponding computer generated δ' particle distribution based on Eqs. (19) through (22).

For aluminum-lithium alloys which have ordered, coherent, spherical particles of uniform diameter d, which are distributed in a triangular array on the slip plane the interparticle spacing λ is given by the following expression [38]

$$\lambda = 1.075/(N_A)^{0.5} - \pi d/4 \tag{23}$$

where N_A is the number of particles intersected per unit area of slip plane. In terms of the average particle size diameter d and volume fraction, interparticle spacing λ is given by [38]

$$\lambda = 0.538\, d(2\pi/3f_v)^{0.5} - \pi d/4 \tag{24}$$

where d is the average particle size diameter, and f_v is the volume fraction of the precipitates.

As the precipitates coarsen, their spacing increases concurrently with their size (see Fig. 6). Eventually they will reach a critical particle size where the dislocation looping of particles becomes easier than dislocation shearing of particles. The minimum radius for Orowan looping is achieved when the particle size reaches the point of equality in the force balance between the stress for precipitate shearing and Orowan looping. At the limit between these two processes, the strengthening for some alloy systems goes through a maximum. However, for some systems the maximum in strength occurs prior to the particle shearing-looping transition. Before there is Orowan looping for all of the particles of the size distribution, there is a transition in which both Orowan looping and particle shearing simultaneously occur for a given distribution. The precipitates are never monodispersed because of the statistical distribution of particle sizes in which large precipitates are bypassed and the dislocations shear looped and small precipitates. The Orowan looping radius can be measured from the size of the smallest Orowan loops observed by TEM on plastically deformed alloys or deduced from the mean precipitate size of the δ' particle size distribution at maximum strength.

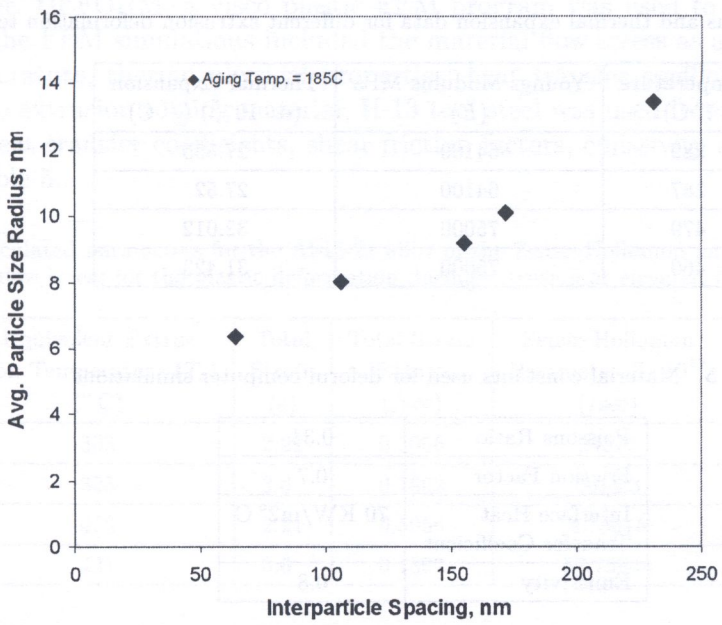

Fig. 6. Comparison between the experimentally measured average $\delta'(Al_3Li)$ particle size radius and the experimentally measured $\delta'(Al_3Li)$ interparticle spacing for the Al-2.6wt. % Li-0.09wt. % Zr alloy aged at 185° C

5.2. Material behavior modeling

The flow stress values, which define the plastic flow behavior of the metal, were calculated from an empirical relation and are summarized in the Table 8. The material constants used to calculate the flow stress values are tabulated in Table 3 [39]. The elastic and the thermal properties of the material were also calculated for various temperatures and tabulated in Tables 2, 4, 6, 7 and 9. Finite element method simulations were conducted to determine the effect of extrusion speed, temperature and die geometry on temperature transients, strain rate, strain and metal flow uniformity in the

Table 2. Comparison between the thermal expansion data for pure aluminum and the Al-Li-Zr alloy

Temperature (K)	CTE pure Al(/K)·10^{-6} (α_e)	CTE Al-Li-Zr alloy (/K)·10^{-6} (α_e)
293	23	22.6167
350	24.1	23.6983
400	24.9	24.485
500	26.5	26.0583
600	28.2	27.73
700	30.4	29.8933
800	33.5	32.94167
900	37.3	36.6783

Table 3. Material constants used for Zener–Hollomon parameter and deform simulations

A	$\alpha*$ Mpa-1	n	Q_{def} KJ/mol
3.848 · 1014	0.01	6.087	184

Table 4. Elastic modulus and thermal expansion data for different extrusion deformation temperatures

Temperature (° C)	Youngs Modulus MPa (E)	Thermal Expansion ($\alpha \cdot 10^{-6}$) (/° C)
289	64100	27.555
287	64100	27.52
479	75000	32.012
460	75000	31.423

Table 5. Material constants used for deform computer simulations

Poissons Ratio	0.34
Friction Factor	0.7
Interface Heat Transfer Coefficient	70 KW/m2° C
Emissivity	0.8

Table 6. Thermal conductivity and heat capacity data for the aluminum-lithium-zirconium alloy at different extrusion deformation temperatures

Temperature T_o (° C)	Thermal Conductivity K (W/m K)	Heat Capacity C (KJ/Kg K)
289	84	3.4744
287	84	3.472
479	72.36	3.70847
460	73.69	3.68495

Table 7. Comparison between the thermal conductivity data for pure aluminum and Al-Li-Zr alloy

Temperature (K)	Thermal Conductivity of Pure Al (W/m K)	Thermal Conductivity of Al-Li-Zr alloy (W/m K)
298.2	237	88
300	237	88
323.2	239	90
350	240	91
373.2	240	91
400	240	91
473.2	237	88
500	236	87
573.2	233	84
600	231	82
673.2	226	77
700	225	76
773.2	219	70
800	218	69
873.2	212	63
900	210	61
933.52	208	59

Al-Li alloy billet. DEFORM, a visco plastic FEM program was used to perform the simulations. Input data for the FEM simulations included the material flow stress as a function of strain, strain rate, and temperature; thermo physical properties; heat transfer coefficients; and friction factor. The data for the extrusion tooling material, H-13 tool steel was used from a materials website [40]. The values of heat transfer coefficients, shear friction factors, emissivity and convection coefficient are listed in Table 5.

Table 8. Calculated parameters for the Al-Li-Zr alloy of the Zener–Hollomon parameters, strain rate, and flow stress for the plastic deformation during extrusion at elevated temperature

Equivalent Extrusion Temperature (T_e) (° C)	Total Strain (ε)	Total Strain Rate ε' (/sec)	Zener–Hollomon Parameter $Z \cdot 10^{12}$ (/sec)	Flow Stress (σ) MPa
303	2.21	0.5056	24577	143.45
303	3.6	0.7802	6013.3	123.34
468	2.21	0.5056	4.73015	46.813
421	3.6	0.7802	57.75944	67.895

Table 9. Comparison of the heat capacity data of pure Al vs. Al-Li-Zr alloy at elevated temperatures

Temperature (K)	Heat Capacity of Pure Al (KJ/Kg K)	Heat Capacity of Al-Li-Zr alloy (KJ/Kg K)
293	0.89598	1.16267
300	0.902	1.16869
373	0.93631	1.203
400	0.949	1.21569
500	0.997	1.26369
560	1.024	1.29069
561	1.02445	1.29114
562	1.0249	1.29159
600	1.042	1.30869
733	1.10318	1.36987
749	1.11054	1.37723
752	1.11192	1.37861
800	1.134	1.40069
1000	0.921	1.18769
1200	0.921	1.18769

The deformation of the billet was assumed to be axi-symmetric, that is the geometry radiating out from the centerline is identical. Due to the symmetry of the extrusion process, the deformation of the right half of the ingot by the right half of the die was considered. Thus, the data for the object, is inputted in the preprocessor, generated and saved. Depending on the difficulty of extrusion, the process is run through a specified number of steps. The results are viewed, captured and saved in the post processor. Simulations for two different die diameters 53 mm and 26.9 mm at different temperatures and ram speeds are carried out.

6. Material data

6.1. Plastic data

For studying the plastic deformation of a given metal it is appropriate to consider uniform or homogeneous deformation conditions. The yield stress of a metal under uniaxial conditions as a function of strain (ε), strain rate (ε') and temperature (T_e) can also be considered as flow stress. The metal starts flowing or deforming plastically when the applied stress reaches the value of yield stress. The values are entered in a tabular data format of strain, strain rate and temperature for which the flow stress values are available. The values of flow stress, which are used in the present simulations, are tabulated in Table 8.

6.2. Elastic data

Elastic data is required for the deformation analysis of elastic and elasto-plastic materials. The three variables are:

(1) *Thermal expansion*: The coefficient of thermal expansion defines the volumetric strain due to changes in temperature. It can be defined as a constant or as a function of temperature. The coefficient of thermal expansion of aluminum alloy at certain temperature is the product of the alloy constant and the coefficient of thermal expansion of pure aluminum at that temperature and is tabulated in Table 2. Based on this concept the thermal expansion of Al-Li-Zr alloy at different temperatures was found from a known value of pure aluminum at that temperature. The values of thermal expansion used in present simulation are tabulated in Table 4.

(2) *Young's Modulus*: Young's Modulus is used for elastic materials and elasto plastic materials below the yield point. It can be defined as constant or as a function of temperature, density (for powder metals). The values of Young's Modulus for the present simulations are given in the Table 4.

(3) *Poisson's ratio*: Poisson's ratio is the ratio between axial and transverse strain. It is required for elastic and elasto-plastic materials. It can be defined as a constant or as a function of temperature. The value for the Poison's ratio used in the present simulations is given in the Table 5.

6.3. Emissivity

The emissive power, E, of a body is the total amount of radiation emitted by a body per unit area and time. The emissivity, ε, of a body is the ratio of emissive power of a given body to the emissive power of a perfect black body. The emissivity value used in present simulation is tabulated in Table 5.

6.4. Thermal conductivity

Conduction is the process by which heat flows from a region of higher temperature to a region of lower temperature within a medium. The thermal conductivity in the present case is the ability of the material in question to conduct heat with in the object. The value can be a constant or a function of temperature. Based on the concept that the thermal conductivities of aluminum alloy and that of the pure aluminum alloy form a family of parallel curves [41], the thermal conductivity of Al-Li-Zr alloy at any temperature can be found from a known value of thermal conductivity of pure aluminum at that temperature and are tabulated in Table 7. The values of the thermal conductivity used in present simulations are tabulated in Table 6.

6.5. Heat capacity

The heat capacity for a given material is the measure of the change in internal energy per degree of temperature change per unit volume. This value can be a constant or a function of temperature. The heat capacity of pure aluminum increases linearly from room temperature. The data to find the effect of alloying addition to pure aluminum is limited but it was found that the heat capacities of aluminum and aluminum alloys form a family of parallel curves [41]. Based on this, the heat capacity of Al-Li-Zr alloy at any temperature can be calculated from a known value of pure aluminum at that temperature. The heat capacity values for Al-Li-Zr alloy found from the values of heat capacity of pure aluminum are tabulated in Table 9. The values of heat capacity used for the extrusion deformation simulations are tabulated in Table 6.

7. Results and discussion

7.1. Computer simulation results

Finite element analysis was used for this purpose performing computer simulations of the plastic deformation during the extrusion. The extrusion of a billet with 152.4 mm initial diameter, 9.1 extrusion ratio, 3.0833 mm per sec ram speed with processing conditions $\varepsilon = 2.21$, $\varepsilon' = 0.5057$/sec is simulated. The contours for these simulations showing the distribution of effective stress, effective strain, effective strain rate, temperature transients, damage, velocity, and load are identified by Fig. 7. Figure 8 shows the line contours for the simulation of the extrusion of a billet with an initial billet temperature of $T_o = 287°$ C. The extrusion of a billet with 152.4 mm initial diameter, 36.5 extrusion ratio, 1.733 mm per sec ram speed with processing conditions, $\varepsilon = 2.21$, $\varepsilon' = 0.5057$ per sec is simulated. The deform simulations showing the distribution of effective stress, effective strain, effective strain rate, temperature transients, deformation damage, velocity and load are shown in Figs. 9 to 12.

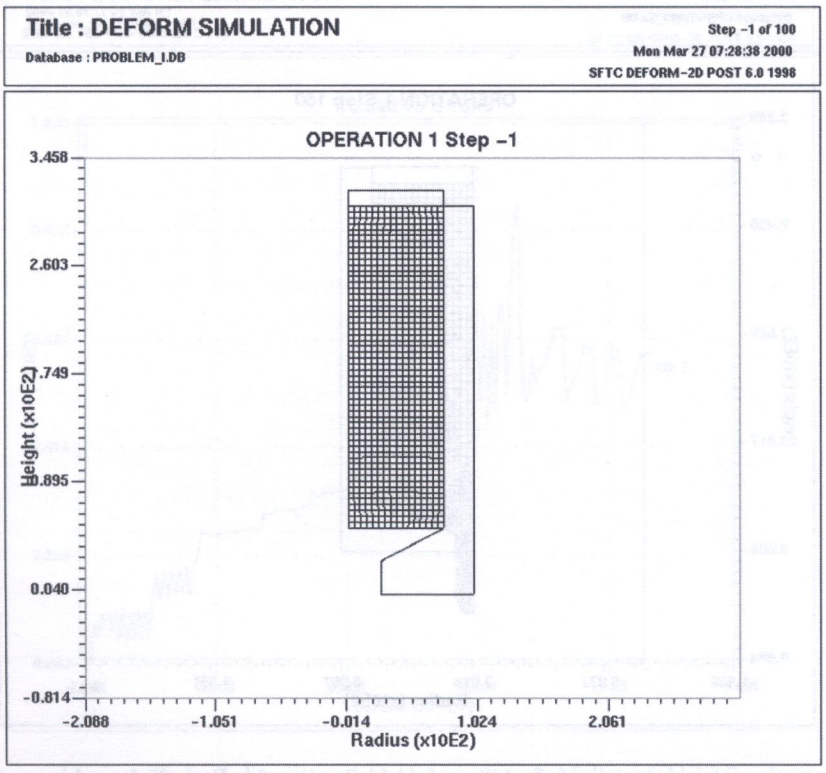

Fig. 7. Contour showing the tooling and billet geometry for $R_e = 9.1$, $T_o = 289°$ C

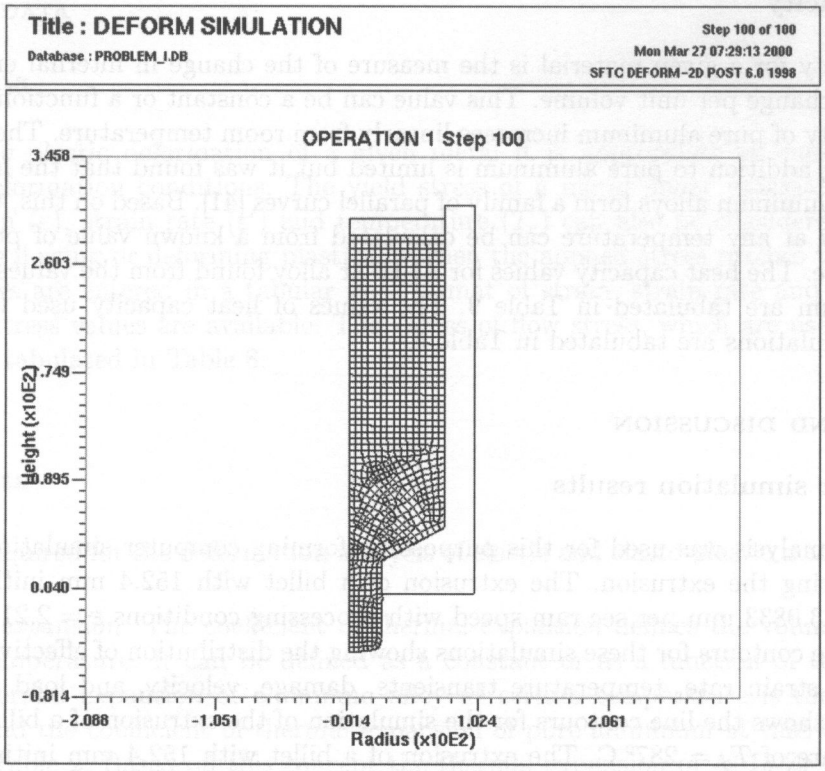

Fig. 8. Mesh showing the extrusion of the billet of Al-Li-Zr alloy for $R_e = 9.1$; and processing conditions: $\varepsilon' = 0.505667\,\mathrm{s}^{-1}$, $\varepsilon = 2.21$, $T_o = 289°\,\mathrm{C}$

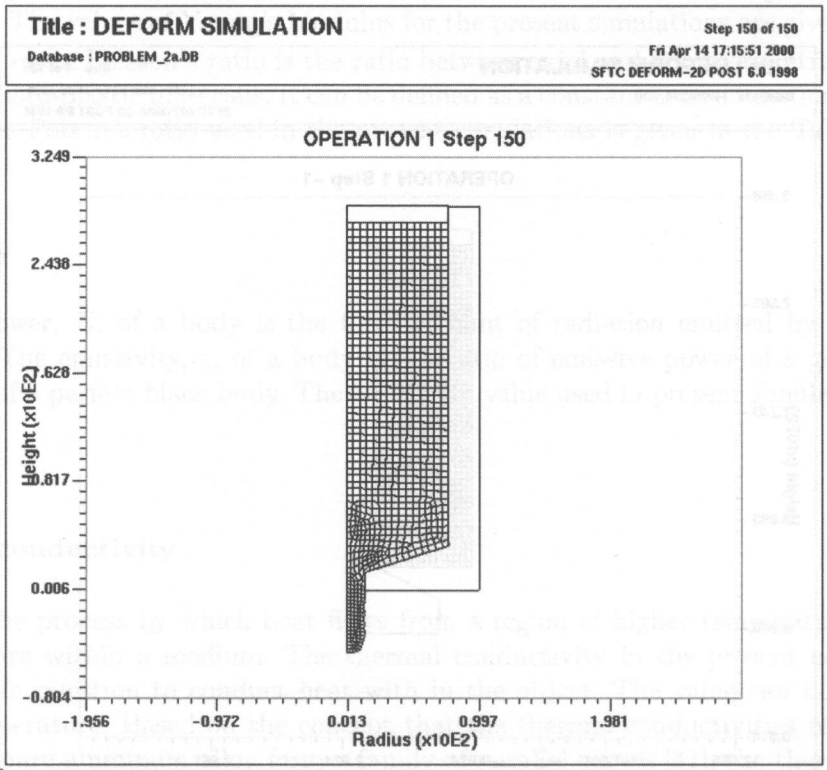

Fig. 9. Mesh showing the extrusion of the billet of Al-Li-Zr alloy for $R_e = 36.5$; and processing conditions: $\varepsilon' = 0.7802\,\mathrm{s}^{-1}$, $\varepsilon = 3.6$, $T_o = 460°\,\mathrm{C}$

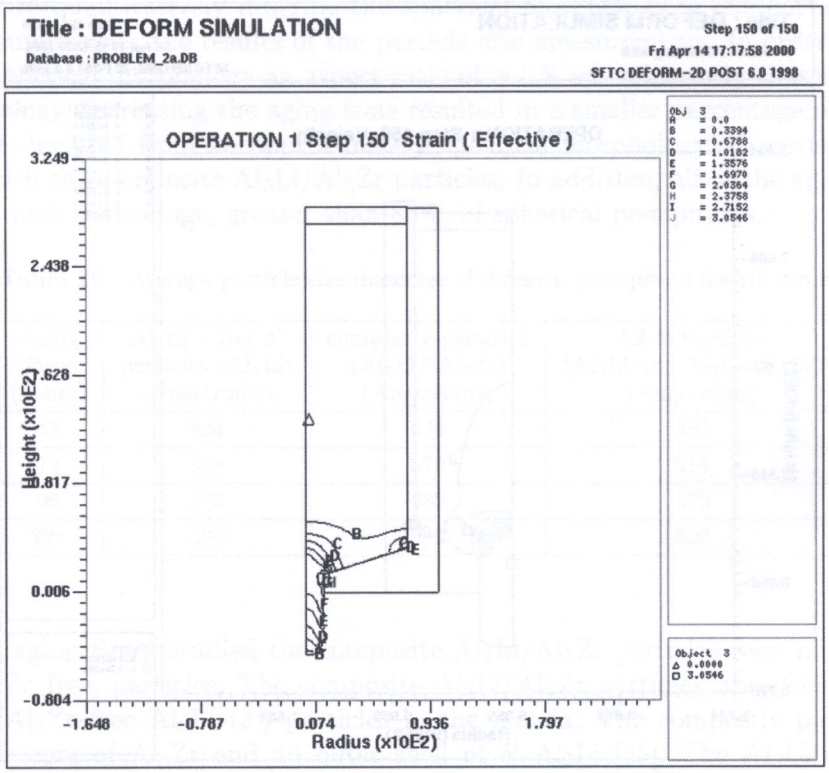

Fig. 10. Contour showing the strain distribution in the as extruded billet of Al-Li-Zr alloy for $R_e = 36.5$; and processing conditions: $\varepsilon' = 0.7802\,\mathrm{s}^{-1}$, $\varepsilon = 3.6$, $T_o = 460°$ C

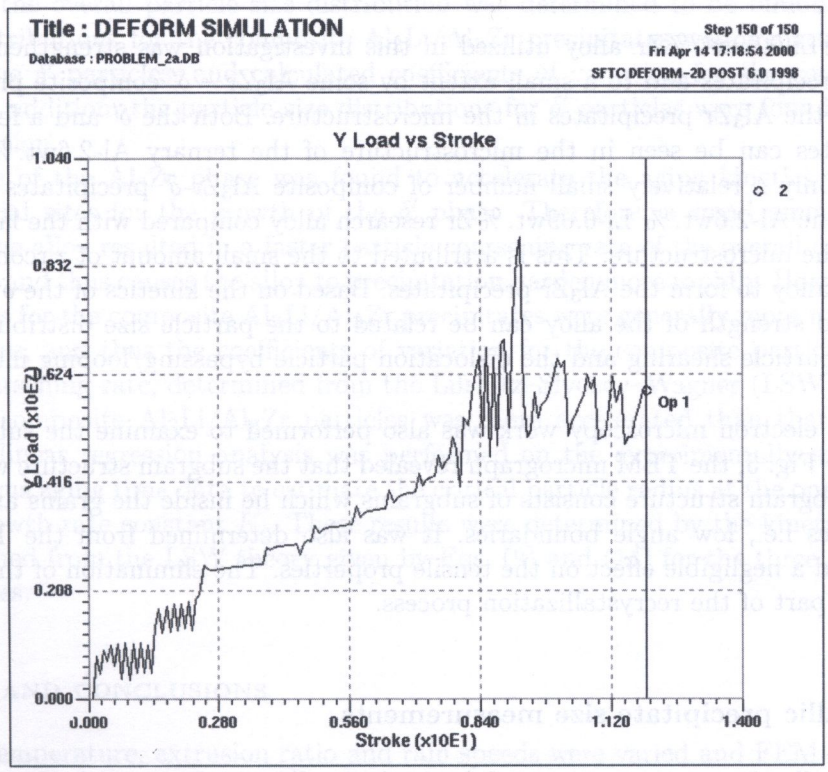

Fig. 11. Contour showing the load distribution in the as extruded billet of Al-Li-Zr alloy with $R_e = 36.5$; and processing conditions: $\varepsilon' = 0.7802\,\mathrm{s}^{-1}$, $\varepsilon = 3.6$, $T_o = 460°$ C

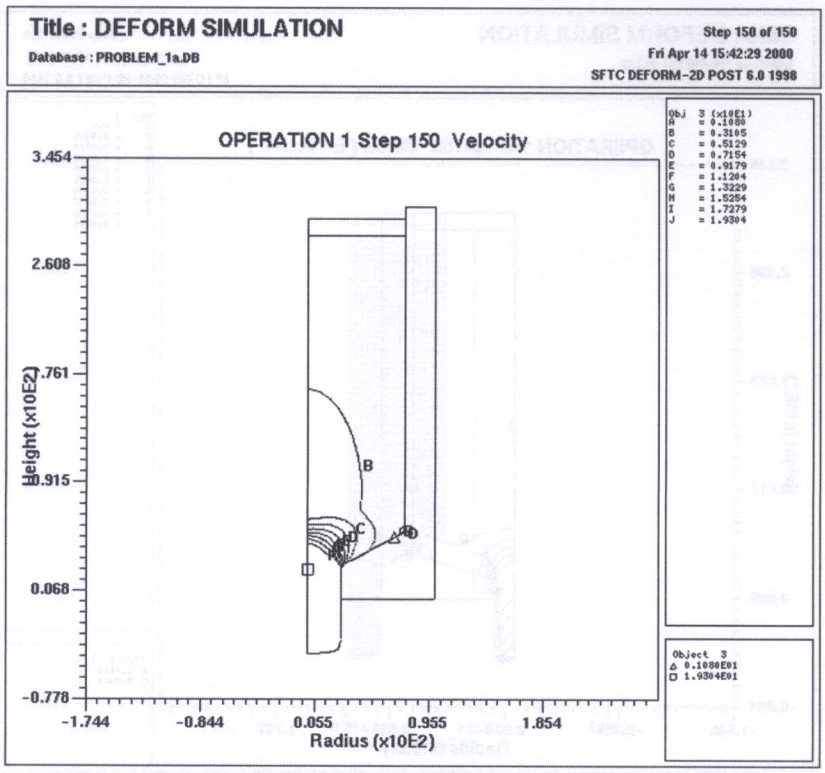

Fig. 12. Contour showing the velocity distribution in the as extruded billet of Al-Li-Zr alloy for $R_e = 9.1$; and processing conditions: $\varepsilon' = 0.505667\,\mathrm{s}^{-1}$, $\varepsilon = 2.21$, $T_o = 479°\,\mathrm{C}$

7.2. TEM microstructure

The Al-2.6wt. % Li-0.09wt. %Zr alloy utilized in this investigation was strengthened primarily by the δ' (Al_3Li) precipitates and to a small extent by some Al_3Zr – δ' composite precipitates where the phase coats the Al_3Zr precipitates in the microstructure. Both the δ' and a few Al_3Zr-δ' composite precipitates can be seen in the microstructure of the ternary Al-2.6wt. % Li-0.09wt. % Zr research alloy. Only a relatively small number of composite Al_3Zr-δ' precipitates exist in the microstructure of the Al-2.6wt. % Li-0.09wt. % Zr research alloy compared with the large number of δ' precipitates in the microstructure. This is attributed to the small amount of zirconium (0.09wt. %) available in the alloy to form the Al_3Zr precipitates. Based on the kinetics of the δ' particle growth the ductility and strength of the alloy can be related to the particle size distribution in terms of the dislocation particle shearing and the dislocation particle bypassing/looping interaction mechanisms.

Transmission electron microscopy work was also performed to examine the subgrain structure. As illustrated by Fig. 3, the TEM micrograph revealed that the subgrain structure was generally not uniform. The subgrain structure consists of subgrains which lie inside the grains and are separated by subboundaries i.e., low angle boundaries. It was also determined from the TEM study that subgrain size had a negligible effect on the tensile properties. The elimination of the subboundaries is an important part of the recrystallization process.

7.3. Intermetallic precipitate size measurements

Particle size distributions were constructed for both the δ' precipitates and the composite precipitates as well as the combined bimodal distribution for all the particles. Two particle diameters were measured for each particle in order to determine the aspect ratio of each particle. The aspect

ratios were used to quantitatively describe the spherical morphology of the particle size distributions. Table 10 summarizes the results of the particle size measurements. In order to estimate any deviation from spherical morphology an aspect ratio of $\geqslant 0.8$ was arbitrarily chosen as indicative of spherical morphology. Increasing the aging time resulted in a smaller percentage of δ', Al_3Zr – free precipitates that deviated from an approximately spherical morphology. However, this trend was not as evident with the composite Al_3Li/Al_3Zr particles. In addition, all of the aging times studied produced a very high percentage, greater than 80%, of spherical precipitates.

Table 10. Average particle size diameter of different precipitate distributions

Aging Time (hours)	Al_3Zr – free δ' particles (Al_3Li) (Angstroms)	composite particles (Al_3Li/ Al_3Zr) (Angstroms)	All δ' particles (Al_3Li and Al_3Li/Al_3Zr) (Angstroms)
48	294	644	303
72	306	670	315
96	303	682	472
225	590	985	600

For all of the aging times studied the composite Al_3Li/Al_3Zr particles were much larger in size than the δ', Al_3Zr–free, particles. The composite Al_3Li/Al_3Zr particles were found to coexist directly with the Al_3Zr–free Al_3Li (δ') particles in the matrix. The composite particles consist of a spherical inner core of Al_3Zr and an outer shell of δ' Al_3Li [35]. The Al_3Li is known [35] to nucleate directly on the existing Al_3Zr particles. There was a very small number of the composite Al_3Li/Al_3Zr precipitates in comparison with the δ', Al_3Zr free, precipitates. The particle size distributions of the composite precipitates were however more skewed toward larger particle sizes. The composite particles shifted the overall particle size distribution to the right of the central maximum, and the overall particle size distribution was determined to be bimodal. However, the particle size distributions for the composite Al_3Li/Al_3Zr precipitates were generally more narrow than those of the δ' particles, and calculated coefficients of variation for the composite particles were smaller. In addition, the particle size distributions for δ' particles were found to resemble the Weibull distribution.

The presence of the Al_3Zr phase was found to accelerate the aging kinetics of the alloy and act as preferential sites for the growth of the δ' phase. Therefore, a small amount of zirconium (0.09wt. %) in the alloy resulted in a faster particle coarsening rate of the overall combined particle size distribution and thus causes the alloy to precipitation harden more rapidly. However, the particle size distributions for the composite Al_3Li/Al_3Zr precipitates were generally more narrow than those of the δ' particles, and thus the coefficients of variation for the composite particles were smaller. The particle coarsening rate, determined from the Lifshitz–Slyozov–Wagner (LSW) coarsening rate theory, for the composite Al_3Li/Al_3Zr particles was more accelerated than that of the δ' Al_3Li precipitates. A linear regression analysis was performed on the experimentally measured average particle size versus aging time data to estimate the critical particle radius at the onset of coarsening, R_{co}, and the growth rate constant K_c. These results were determined by the kinetic law defined by Eq. (8) determined from the LSW theory given by Eqs. (9) and (14) for the three different particle distribution types.

8. Summary and conclusions

The extrusion temperature, extrusion ratio and ram speeds were varied and FEM simulations were conducted to determine the effect of these extrusion parameters on temperature transients, strain rate and metal flow uniformity for the high temperature plastic deformation of Al-Li alloy billet. Deform, a visco plastic FEM program was used for this purpose.

From the deform computer simulations conducted for different extrusion processing conditions of the Al-Li-Zr alloy, various conclusions were determined from the research. The FEM simulations were important in determining temperature transients; metal flow patterns and the distribution of strain and strain rate. The contours show that the strain, strain rate and metal flow were not uniform but varied as the billet was extruded, this might be due to the non-uniform distribution of temperature in the as-extruded billet. For almost the same billet temperatures, but different ram speeds the billet with higher extrusion ratio was found to have greater strain rate than that of the billet with lower extrusion ratio. At the entrance of the die orifice, the billet with 36.5 extrusion ratio was found to have a strain rate of 2.046 per second, where as it was only 1.223 per second for the billet extruded at 9.1 extrusion ratio. The strain rate at the surface of the billet was found to be greater than the strain rate at the core. The plots of effective strain and strain rate indicated that the maximum strain and strain rate occurred at the die orifice and slowly decreased as the billet is extruded. The strain rate distribution was found to be almost similar for the billet extruded at different temperatures but with the same processing conditions i.e., with the same ram speeds and extrusion ratio.

For almost the same initial billet temperatures but different ram speeds, the exit temperature of the billet with higher extrusion ratio was found to be more than the exit temperature of the billet with lower extrusion ratio when the billet was at a higher temperature than the container. In the case when the billet was at a higher temperature than that of the container, the initial temperature of the billet was found to be the maximum temperature of the billet. In the case when the billet was at a higher temperature than the container, the temperature increased in the beginning but later fell as the billet was extruded. In the above mentioned case when the billet was at higher temperature than the container, the temperature of the surface of the billet in contact with the container was less than the core temperature. Whereas in the case when the billet was at a lower temperature than the container, the surface temperature of the billet in contact with the container was more than the core temperature of the billet. The flow stress of the material was observed to decrease with an increase in temperature. The flow stress value of the billet material for the equivalent temperature equal to 303° C, was found to be 143.5 MPa, whereas it was only 46.8 MPa for the billet with equivalent temperature equal to 468° C. The effective stress was found to be more at the surface than at the core. The velocity of the metal flow was found to be more at the center of the billet than at the peripheral region. For the billet extruded at a temperature 289° C, the velocity of the metal flow at the center of the billet was found to be 6.98 mm per second whereas it was 2.82 mm/s at the peripheral. The velocity of the metal flow was found to be almost zero at the dead metal zone. The load exerted by the ram on the billet at the end of the extrusion when it was extruded at a temperature of 289° C with an extrusion ratio of 9.1 was found to be 10,360 KN. The load exerted by the ram on the billet at the end of the extrusion when it was extruded at a temperature of 287° C with an extrusion ratio of 36.5 was found to be 11400 KN. The load exerted by the ram on the billet at the end of the extrusion when the billet was extruded at a temperature of 479° C with an extrusion ratio of 9.1 was found to be 2904 KN. The load exerted by the ram on the billet at the end of the extrusion when the billet was extruded at a temperature of 460° C with an extrusion ratio of 36.5 was found to be 5824 KN. For the same extrusion parameters the load required for the billet extruded at a lower temperature was higher than the load required for the billet extruded at a higher temperature.

The Zener–Hollomon parameters for the Al-2.6wt. % Li-0.09wt. % demonstration alloy were determined from the extrusion processing variables and correlated to the average subgrain sizes. The average equivalent temperatures were determined for the various extrusions and used for the calculations of the Zener–Hollomon parameters. The values of the activation energy for deformation and the equivalent extrusion temperatures were approximated and used for the estimations of Z. The measured subgrain sizes were found to increase with the solution heating. For any given extrusion temperature there was an inverse relationship between the measured subgrain size and the $\ln(Z)$. Smaller grain sizes were correlated to larger Zener–Hollomon parameters. Based on optical and electron microscopy studies it was found that regardless of the extrusion conditions, the various microstructures for the most part were unrecrystallized for both the as-extruded and the solution heat treated conditions.

Acknowledgements

The aluminum-lithium alloy used for this study was provided by the Aluminum Company of America (ALCOA) and cast by the ALCOA Technical Center in Pittsburgh Pennsylvania, USA. The Al-Li alloy was extrusion processed by the ALCOA Lafayette Extrusion and Tube Division in Lafayette, Indiana, USA. The composition analysis for the Al-Li alloy was also performed by the ALCOA Extrusion Facility, Lafayette, Indiana, USA. This work was supported in part by funding through the National Science Foundation.

References

[1] M. M. Farag, C. M. Sellars. Flow stress in hot extrusion of commercial purity aluminum. *Journal of the Institute of Metals*, **101:** 137–145, 1973.

[2] A. F. Castle, T. Sheppard. Pressure required to initiate extrusion in some aluminum alloys. *Metals Technology*, 465–475, 1976.

[3] D. Raybould, T. Sheppard. Axisymmetric extrusion: the effect of temperature rise and strain rate on the activation enthalpy and material constants of some aluminum alloys and their relation to recrystallization, substructure, and subsequent mechanical properties. *Journal of the Institute of Metals*, **101:** 65–72, 1973.

[4] P. Feltham. Extrusion of metals: a simple theory of criteria of press design and extrusion efficiency in the industrial extrusion of metals. *Metal Treatment and Drop Forging*, **23:** 440–444, 1956.

[5] G. E. Dieter. Extrusion, Mechanical Metallurgy. *McGraw-Hill, Inc.*, 616–635, 1986.

[6] H. J. McQueen, J. J. Jones. Recent advances in hot working fundamental dynamic softening mechanisms. *Journal of Applied Metal Working*, **3:** 3, 233–241, 1984.

[7] T. Sheppard. Temperature and speed effects in hot extrusion of aluminum alloys. *Metals Technology*, 130–141, 198.

[8] C. M. Sellars. Hot working operations. *Aluminum Transformation Technology and Applications, American Society for Metals*, 405–440, 1978.

[9] C. M. Sellars. *Aluminum Transformation Technology and Applications*, 405–440, 1978.

[10] H. J. McQueen, J .J. Jonas. Treatise on material science and technology. *Academic Press*, **6:** 404, New York, 1975.

[11] H. J. McQueen, J. J. Jonas. Plastic deformation of materials, R.J. Arsenault, (ed.). *Academic Press*, New York.

[12] J. H. Kulwicki, T.H. Sanders, Jr. Coarsening of δ' (Al_3Li) precipitates in an Al-2.7Li-0.3Mn alloy. *Aluminum-Lithium Alloys II*, 31–51, 1986.

[13] S. F. Baumann, D. B. Williams. A new method for the determination of the precipitate-matrix interfacial energy. *Scripta Metallurgica*, **18:** 611–616, 1984.

[14] I. M. Lifshitz, V. V. Slyozov. The kinetics of precipitation from supersaturated solid solutions. *Journal Physical Chemical Solids*, **19:** 35–50, 1961.

[15] C. Wagner. Theories associated with age hardening and overaging during ostwald ripening (in German). *Zeitschrift fur Elekrochemie*, **3:**(7), 581–591, 1961.

[16] J. C. Huang. Microstructural evolution and strengthening mechanisms in two ternary Aluminum-Lithium-Copper alloys. *Ph.D. Dissertation, University of California*, Los Angeles, 1986.

[17] A. J. Ardell. The effect of volume fraction on particle coarsening: theoretical considerations. *Acta Metallurgica*, **20:** 61–71, 1972.

[18] A. D. Brailsford, P. Wynblatt. The dependence of ostwald ripening kinetics on particle volume fraction. *Acta Metallurgica*, **27:** 489–497, 1979.

[19] C. K. L. Davies, P. Nash, R. N. Stevens. The effect of volume fraction of precipitate on ostwald ripening. *Acta Metallurgica*, **28:** 179–189, 1980.

[20] B. P. Gu. Coarsening kinetics of Al_3Li (δ') precipitates in Al-Li alloys. *Ph.D. Dissertation*, Purdue University, 1985.

[21] H. R. Shercliff, M. F. Ashby. Modelling of the response of heat-treatable aluminum alloys to thermal processing. *Report CUED/C-Mat./TR156*, Cambridge University Engineering Department, 1989.

[22] B. P. Gu, S. C. Jha, G. L. Liedl, K. Mahalingam, T. H. Sanders, Jr. Microstructure and the behavior of Aluminum-Lithium alloys. *Light Metals*, 35–43, 1985.

[23] B. P. Gu, G. L. Liedl, T. H. Sanders, Jr., K. Welpmann. The influence of zirconium on the coarsening of δ' (Al_3Li) in an Al-2.8wt. % Li-0.14wt. % Zr alloy. *Material Science and Engineering*, **76:** 147–157, 1985.

[24] B. P. Gu, K. Mahalingam, G. L. Liedl, T. H. Sanders, Jr. The δ' (Al_3Li) particle size distribution in a variety of Al-Li alloys. *Aluminum-Lithium Alloys III*, 360–368, 1986.

[25] B. P. Gu, G. L. Liedl, K. Mahalingam, T. H. Sanders, Jr. Application of the Weibull density function to describe the δ' (Al_3Li) particle size distribution in binary Al-Li alloys. *Material Science and Engineering*, **78:** 71–85, 1986.

[26] B. P. Gu, G. L. Liedl, K. Mahalingam, T. H. Sanders, Jr. Coarsening phenomenon in Aluminum-Lithium alloys. *Unusual Techniques and New Applications of Metallography*, **24**, 1986.

[27] S. C. Jha, K. Mahalingam, T. H. Sanders, Jr. Analytical models to predict the microstructure of binary Al-Li alloys. *Aluminum Alloys: Their Physical and Mechanical Properties*, **2**, 677–693, 1986.

[28] S. C. Jha, T. H. Sanders, Jr., M. A. Dayananda. Grain boundary precipitate free zones in Al-Li alloys. *Acta Metallurgica*, **35:**(2), 473–482, 1987.

[29] S. C. Jha. Precipitation processes in Al-Li and Al-Li-Mg alloys. *Ph.D. Dissertation*, Purdue University, 1987.

[30] O. Jensrud, N. Ryum. The development of microstructures in Al-Li alloys. *Materials Science and Engineering*, **64:** 229–236, 1984.

[31] D. B. Williams, J. W. Edington. The precipitation of δ' (Al_3Li) in dilute Aluminum-Lithium alloys. *Metal Science Journal*, **9:** 529–532, 1975.

[32] K. Mahalingam, B. P. Gu, G. L. Liedl, T. H. Sanders, Jr. Coarsening of δ' (Al_3Li) precipitates in binary Al-Li alloys. *Acta Metallurgica*, **35:**(2), 483–498, 1987.

[33] K. Mahalingam. Precipitation behavior of δ' in binary Aluminum-Lithium alloys. *Ph.D. Dissertation*, Purdue University, 1989.

[34] K. Dinsdale, S. J. Harris, B. Noble. Aluminum-Lithium alloys. *Philadelphia, PA: The Metallurgical Society of A.I.M.E.*, **101**, 1981.

[35] F. W. Gayle, J. B. Vander Sande. Composite precipitates in an Al-Li-Zr alloy. *Scripta Metallurgica*, **18:** 473–478, 1984.

[36] E. Starke, Jr., T. H. Sanders, Jr., I. G. Palmer. New approaches to alloy development in the Al-Li system. *Journal of Metals*, **33:** 24–33, 1981.

[37] T. H. Sanders, Jr., E. A. Starke, Jr. The effect of slip distribution on the monotonic and cyclic ductility of Al-Li binary alloys. *Acta Metallurgica*, **30:** 927–939, 1982.

[38] J. F. Nie, B. C. Muddle, I. J. Polmear. The effect of precipitate shape and orientation in dispersion strengthening in high strength aluminum alloys. *Materials Science Forum*, **217-222:** 1257–1262, 1996.

[39] V. K. Jain, K. V. Jata, J. T. Morgan, A. K. Hopkins. Ingot breakdown of an Aluminum-Lithium alloy. *Light Weight Alloys for Aerospace Applications III, E. W. Lee, N. J. Kim, K. V. Jata, and W. E. Frazier (Ed.), The Minerals, Metals & Material Society*, 227–243, 1995.

[40] http://www.matls.com

[41] J. E. Hatch. Aluminum: properties and physical metallurgy. *American Society for Metals*, Metals Park, Ohio, 200-241.